HHS Public Access

Author manuscript

*Adv Mater*. Author manuscript; available in PMC 2023 July 01.

Published in final edited form as:

*Adv Mater*. 2022 July ; 34(30): e2200512. doi:10.1002/adma.202200512.

# Multiphoton Lithography of Organic Semiconductor Devices for 3D Printing of Flexible Electronic Circuits, Biosensors, and Bioelectronics

**Omid Dadras-Toussi**,

**Milad Khorrami**,

**Anto Sam Crosslee Louis Sam Titus**,

**Sheereen Majd**,

**Chandra Mohan**,

**Mohammad Reza Abidian**

Department of Biomedical Engineering, University of Houston, 3517 Cullen Blvd, Houston, TX 77204, USA

## Abstract

In recent years, 3D printing of electronics have received growing attention due to their potential applications in emerging fields such as nanoelectronics and nanophotonics. Multiphoton lithography (MPL) is considered the state-of-the-art amongst the microfabrication techniques with true 3D fabrication capability owing to its excellent level of spatial and temporal control. Here we introduce a homogenous and transparent photosensitive resin doped with an organic semiconductor material (OS) compatible with MPL process to fabricate variety of 3D OS composite microstructures (OSCMs) and microelectronic devices. Inclusion of 0.5 wt% OS in the resin enhanced the electrical conductivity of the composite polymer about 10 orders of magnitude and compared to other MPL-based methods, the resultant OSCMs offered high specific electrical conductivity. As a model protein, laminin was incorporated into these OSCMs without a significant loss of activity. The OSCMs were biocompatible and supported cell adhesion and growth. Glucose oxidase encapsulated OSCMs offered a highly sensitive glucose sensing platform with nearly 10-fold higher sensitivity compared to previous glucose biosensors. In addition, this biosensor exhibited excellent specificity and high reproducibility. Overall, these results demonstrate the great potential of these novel MPL-fabricated OSCM devices for a range of applications from flexible bioelectronics/biosensors, to nanoelectronics and organ-on-a-chip devices.

## Abstract

mabidian@uh.edu .

Supporting Information

Supporting Information is available from the Wiley Online Library or from the author.

Conflict of Interest

The authors have no conflict of interest

3D printing of flexible microelectronics has gained significant attention. Here, a photosensitive resin doped with organic semiconductor material is developed for direct laser writing based on multiphoton lithography. Fabrication of microelectronic devices, hybrid microelectrodes, cell-adhesive substrates, and high-performance glucose biosensors are successfully demonstrated. These soft and conductive microstructures have potential in flexible electronics, organic bioelectronics, and biosensors.

## Keywords

Organic semiconductors; Multiphoton lithography; Electronics; Bioelectronics; Biosensors

Development of innovative 3D micro and nanoscale technologies in nanoelectronics[1], micro/nano electromechanical systems[2], nanophotonics[3], micro/nanofluidics[4], and nanobiosciences[5] requires advancements in existing light induced-additive manufacturing techniques including electron beam lithography[6], digital light processing[7], dip pen lithography[8], stereolithography[9], interference lithography[10], and multiphoton lithography (MPL).[11] Among these techniques, MPL based on direct laser writing is state-of-the-art owing to its high spatial and temporal control as well as the versatility of photosensitive materials mostly composed of acrylate-based polymers/monomers or epoxy-based photoresists. One notable feature of MPL is its ability to fabricate 3D microstructures with subwavelength resolution typically 100-200 nm beyond the optical diffraction limit, achieved by combination of threshold effect and reduction of effective beam diameters due to multiphoton adsorption of pulsed femtosecond near infrared laser beams (ca. 800 nm).[12, 13] Precise modulation of laser intensity, together with optimal writing speed and use of high numerical aperture objective lens have even enabled spatial resolution down to 15 nm.[14]

More importantly, MPL is an ideal tool for 3D printing of functional structures using photosensitive composite resins doped with stimuli-responsive nanomaterials. Semiconductive nanoparticles, magnetic nanoparticles, and metallic nanoparticles have been introduced into the resins to fabricate photoluminescent micro-nanostructures[15], remotely controllable micro-nanomachines[16], and conductive micro-nanoarchitectures[17], respectively. However, these nanomaterials that usually exhibit inorganic properties are difficult to disperse homogenously in largely doped fashion within photopolymerizable resins without significant phase separation.[16, 18]

In recent years, there have been significant interests and efforts in fabrication of MPL-based electrically conductive structures due to their potential applications in emerging fields such as nanoelectronics, nanophotonics, plasmonics, and bioelectronics. Metal salts such as $AgNO_3$[19, 20] and $HAuCl_4$[17, 21, 22] with relatively high concentration (≈50 wt%) can be mixed with photoresist and MPL is employed for simultaneous photoreduction of metallic salts and photopolymerization of photoresist to fabricate highly conductive metallic nanoparticle-doped polymeric microstructures. Although relatively high specific electrical conductivities up to ≈$10^6$ S $m^{-1}$ $wt\%^{-1}$ (conductivity per concentration of metallic nanoparticles) can be achieved, metal-nanoparticle-loaded resins produces planar structures.

[17] On the other hand, MPL-compatible composite resins containing carbon nanotubes (CNTs)[23–25] and graphene[26, 27] exhibit 3D microstructures. However, these nanomaterials demonstrate low specific electrical conductivities up to only ≈200 S $m^{-1}$ wt%$^{-1}$[24].

To address these challenges, herein, we report a homogenous, transparent, and stable photosensitive resin doped with an organic semiconductor material (OS) to fabricate highly conductive 3D microstructures with high-quality structural features via MPL process. OSs are a broad family of **π**-conjugated molecules or polymers with alternating single and double bonds. The oxidized OSs (i.e. positively (p) doped) can reach conductivities up to several thousand S $m^{-1}$. To maintain electroneutrality, anions are intercalated within the bulk of p-doped OSs, providing both mobile electronic and ionic charge carriers.[28] Furthermore, OSs have many unique properties such as mixed ionic and electronic conduction, mechanical flexibility, large optical absorption and emission, and solution processability[29, 30] that are crucial for several applications including optoelectronics[31, 32], printed electronics[33, 34], and bioelectronics.[35–38] Poly(3,4-ethylenedioxythiophene) (PEDOT) is considered one of the most promising OSs due to its high electrical conductivity and chemical stability.[39, 40] Fabrication of organic bioelectronics has mostly relied on patterning and/or electrodeposition of OS on metal electrodes that are microfabricated using conventional multi-step lithography methods with limitations and challenges such as low resolution, two-dimensional patterns, and/or complex and high-cost procedures.[41–43]

Here, for the first time we report applying MPL process to directly fabricate 3D organic semiconductor composite microstructures (OSCMs). We introduce a new MPL compatible resin composed of photopolymer poly(ethylene glycol) diacrylate (PEGA), organic semiconductor poly(3,4-ethylenedioxythiophene):poly(styrenesulfonate) (PEDOT:PSS), photoinitiator 3-(trimethoxysilyl)propyl methacrylate (T-POL), and miscible agent dimethyl sulfoxide (DMSO) (Figure 1A, black boxes). Microelectronic devices made of this OS composite resin were fabricated via MPL process and were characterized. Furthermore, proteins such as laminin and glucose oxidase were incorporated (Figure 1A, blue box) within MPL-based conductive microstructures and assessed for their biological activity and functionality. Compared to other 3D printing methods[44] such as ink-jet printing[45], aerosol printing[46], nozzle printing[47], screen printing[48], and lithography[49], MPL offers facile fabrication of OS composite microstructures with high resolution and high aspect ratio that can be integrated with other MPL compatible materials such as insulating polymers to fabricate functional electronic circuits, biosensors and bioelectronics.

Figures 1A–D illustrate the chemical components of the composite resin and the MPL experimental procedure for fabrication of conductive microstructures. The composite resin was prepared by direct addition of a mixture of OS and DMSO to PEGA/T-POL (see resin preparation in the Experimental Section). The reason for choosing DMSO is the miscibility of the OS, PEGA, and T-POL in DMSO in order to prepare a homogeneous and transparent MPL-compatible resin (Figure 1A). It was observed that in the absence of DMSO, OS would immediately aggregate, revealing the importance of DMSO in complete dispersion of OS (Figure S1A, Supporting Information). The photoinitiator T-POL was used due to its water solubility, biocompatibility, high initiation efficiency, and large absorbance wavelength 600-810 nm.[50, 51] To demonstrate its potential application, the OS composite resin was

further modified with proteins such as laminin and glucose oxidase (blue box in Figure 1A) (see resin preparation in the Experimental Section). During the MPL process, a femtosecond laser beam (center wavelength of 780 nm, pulse width of 130 nm, repetition rate of 80 MHz, and power of 20 mW) was tightly focused by an objective lens (40X, numerical aperture (NA) 0.65) into the resin. The sample was then moved by a 3D piezostage to make 3D scans with a speed of 50 μm $s^{-1}$ based on the pre-defined geometric design, resulting in solidified 3D microstructures, while OS was simultaneously incorporated within the polymer (Figure 1B). After MPL fabrication, the samples were rinsed in ethanol for 1 min to remove any unsolidified resin, leaving the 3D microstructures of OS composite polymer on substrates (Figures 1C and 1D).

Resin with DMSO concentration between 25 and 35 wt% was found to be MPL-compatible. Specifically, OS was not miscible in DMSO with concentration below 25 wt%, while further addition of DMSO above 35 wt% into the resin yielded detached and lower quality microstructures (Figures S1B–E, Supporting Information). The prepared resin was stable for ≈30 h at room temperature without obvious OS aggregation (Figure S2, Supporting Information). In addition, the maximum miscibility of OS in the resin was found to be 0.5wt% (Figure S3, Supporting Information). The fabrication process was performed on either flexible polydimethylsiloxane (PDMS) (Figure 2A) or glass substrates. Figures 2B–F and Figure S4 (Supporting Information**)** show some examples of 3D conductive microstructures fabricated from the OS composite resin (0.5 wt% OS), including array of micro-grids, micro-snowflakes, micro-springs, micro-honeycombs, and vertical micro-tubes. It is noteworthy that the feature size (line width) of ≈ 400 nm was achieved when a 28 mW fs laser was focused by an oil immersion objective lens 63X (NA 1.4) and the OS composite resin was scanned with a speed of 100 μm $s^{-1}$ (Figure S5, Supporting Information) . We characterized the optical transparency of the composite resin as a function of OS concentration (Figure 2G). As the concentration of OS increased from 0 to 0.5 wt%, the transmittance decreased from 99% to 89% at 550 nm (Figure 2H), demonstrating an excellent optical transparency for the composite resin. The high level of optical transmittance is an appealing feature for potential optoelectronic application of MPL-fabricated organic semiconductor composite microstructures (OSCMs).

Fourier transform infrared spectroscopy (FTIR) was conducted to confirm that OS was incorporated within 3D microstructures (Figure 3A). For the OS composite polymer microstructures (shown in red curve) and polymer microstructures (shown in black curve), two characteristic peaks were observed at 2910 $cm^{-1}$ and 1724 $cm^{-1}$, which correspond to stretching of –CH and =CO bonds of the polymer, respectively. Furthermore, the OS composite polymer showed three peaks at 1162 $cm^{-1}$, 1121 $cm^{-1}$, and 1066 $cm^{-1}$ that correspond to stretching vibration of ethylenedioxy group, as well as peaks at 1345 $cm^{-1}$ and 1500 $cm^{-1}$, which can be attributed to C-C and C=C bonds in the thiophene ring of pure OS (shown in blue curve). To characterize the electrical conductivity of the OS composite polymers, we fabricated bar-shaped microstructures (265 μm × 10 μm × 10 μm: length × width × height) connecting two pairs of gold (Au) electrodes (Figure S6A, Supporting Information). A Semiconductor Device Parameter Analyzer (B1500A, Keysight) was utilized to obtain the current-voltage (I-V) curves and to calculate the electrical

conductivity of the OS composite microstructures (OSCMs) (Equation S1 and Figure S6B, Supporting Information). Figure 3B shows the electrical conductivity of the OSCMs as a function of different OS concentrations in the resin. As depicted, while the polymer microstructures (without OS) were not conductive, loading as low as 0.1 wt% OS into the resin dramatically increased electrical conductivity of the OSCMs over 8 orders of magnitude (from $2\times10^{-6} \pm 6.5\times10^{-7}$ S $m^{-1}$ to $3\times10^{2} \pm 2\times10^{2}$ S $m^{-1}$). Furthermore, the electrical conductivity significantly increased to $2.7\times10^{4} \pm 6\times10^{3}$ S $m^{-1}$ by increasing the OS concentration to 0.5 wt% (the maximum miscibility concentration of OS in the resin). It is noteworthy that there was statistically significant difference in the electrical conductivities of OSCMs fabricated with 0.1, 0.2, 0.3, 0.4, and 0.5 wt% ($p<0.001$). To further demonstrate the electrical conductivity of the OS composite polymer compared to non-conductive polymer, OS composite polymer fabricated from a resin composed of 0.5 wt% OS with a thickness of 1 mm and conductance of less than 0.1 S was able to serve as an interconnect to switch on a light-emitting diode (Figures 3C and 3D, Movie S1, Supporting Information). The electrical conductivity of the OS composite polymer can be attributed to presence of OS in the cross-linked polymer chains, providing both ionic and electronic conduction pathways along the polymer chains (Figure 3E).[35] Moreover, the excessive increase in electrical conductivity of OSCMs is ascribed to the conductivity enhancing agent DMSO that also acts as a miscible agent. Commercially available OS PEDOT:PSS is an aqueous dispersion of chemically polymerized PEDOT in polyelectrolyte PSS with moderate electrical conductivity (ca. 100 S $m^{-1}$).[39] It has been reported that the use of DMSO could dramatically increase the electrical conductivity of OS (about 2 orders of magnitude)[52–54], presumably due to removal of insulating counterions (i.e. PSS) from OS[55], reducing the columbic interactions between OS and counterions[53], as well as reorientation and conformation of the OS polymer chains.[56, 57] It should be noted that varying the concentration of DMSO in the resin between 25 and 35 wt% (MPL-processible range of DMSO concentration in the resin) did not significantly change conductivity (Figure S7, Supporting Information).

Materials confocal microscopy (MCM) was utilized to assess the surface topography of the OSCMs. As previously shown in the scanning electron micrographs (Figures 2C–F) and indicated in the 3D view of the color-coded height map (Figure 3F), OSCMs (OS 0.5 wt%) had high-quality structural features and were relatively smooth with average surface roughness of 38 nm compared to non-conductive microstructures (Figure S8, Supporting Information). MCM revealed that as the OS concentration increased from 0.1 wt% to 0.5 wt%, surface roughness increased from 19 ± 1.2 nm to 38 ± 1.3 nm ($p<0.001$), respectively (Figure 3G). Moreover, there was statistically significant difference in the surface roughness of OSCMs fabricated with 0, 0.1, 0.2, 0.3, 0.4, and 0.5 wt% OS ($p<0.05$). In addition to the quality of the MPL-based conductive microstructures, the specific conductivity (conductivity per concentration of conductive filler in resin) is a particularly relevant metric for evaluating the efficiency of the fabrication method, especially for large-scale fabrication at low costs (Table S1, Supporting Information). Figure 3H provides a comparison between the specific conductivity of the MPL-fabricated structures in relevant studies using various conductive fillers. High content metallic nanoparticles in the resin such as Au and Ag salts (10-50 wt%) demonstrated high specific electrical conductivity of MPL-based composites ($10^{4}$-$10^{6}$ S $m^{-1}$

wt%$^{-1}$), however, this method often produced planar microstructures.[17, 19–22, 58, 59] In contrast, inclusion of carbon-based nanomaterials in the resin such as CNTs, graphene, and post polymerization of conductive monomers (0.01-10 wt%) yielded 3D microarchitectures with low specific conductivities.[23–27, 60–62] Remarkably, our OSCMs (0.5 wt% OS) not only exhibits high specific conductivity (≈ 5.4×10$^4$ S m$^{-1}$ wt%$^{-1}$) but also smooth surfaces and high-quality 3D structural features (Figures 2C–F, Figures 3F and 3G). The high specific conductivity together with the high-quality 3D microstructures of our OS composite polymer represents a profound improvement in the fabrication of MPL-based 3D conductive architectures compared to previously reported composite resins (Figure 3H).

To demonstrate the potential of MPL fabrication process based on the OS composite resin, we designed, fabricated, and characterized various microelectronic devices, including a micro-printed circuit board (μPCB), which comprises various electrical elements (Figure 3I), and an array of microcapacitors (Figure 3K). The straight lines in the I-V graph (Figure 3J) showed the resistor behavior of elements a1, a2, a3, and a4 (Table S2, Supporting Information) with conductance of 106.52 ± 9.31, 140.16 ± 13.14, 202.54 ± 15.39, and 459.31 ± 44.74 μS (n=5), respectively. Figure 3L shows the hysteresis loop (scan rate: 2 V s$^{-1}$) of an array of microcapacitors (three microcapacitors in parallel, Table S3 Supporting Information). The rectangular-shaped I-V curve indicates capacitor behavior with a specific capacitance of 0.08 ± 0.02 F g$^{-1}$ (n=3) (Equation S2, Supporting Information).

3D bioprinting of OSCMs based on MPL has potential in tissue engineering applications. To demonstrate the versatility of this method, we first formulated and developed a bioactive resin by adding laminin (LM) to the OS composite resin (see resin preparations in Experimental Section). LM was immobilized within OSCMs during solidification of the composite resin. Fluorescent microscopy micrographs shown in Figure 4A and 4B indicate the distribution and incorporation of laminin into M PL-fabricated LM-OSCMs (OS concentration in resin was 0.5 wt%, and LM concentration was 0.1 μM) and line intensity scans across the LM-OSCMs structures revealed a coefficient of variation of 5.5% (Figure S9, Supporting Information). Laminin is a key component of the basement membrane in multiple tissues, and is involved in structural stability, cell attachment, cell signaling, cell migration, cell proliferation as well as angiogenesis.[63, 64] To confirm that the bioactivity of LM was retained throughout the entire MPL process, primary mouse endothelial cells were cultured for 48 h on the LM-OSCMs (500 μm × 500 μm × 2 μm: length × width × height). As shown in the fluorescent micrographs in Figure 4C and 4D, and demonstrated in Figure 4E, the attachment of endothelial cells was significantly higher on LM-OSCMs compared to OS microstructures without laminin (337 ± 20 and 8 ± 13 cells mm$^{-2}$, respectively, $p$<0.001). Cells seeded on LM-OSCMs displayed evidence of adherence to substrate, proliferation, and enhanced survival, whereas the cells barely held on to the substrate and were rounded and non-proliferative on OS microstructures. These results confirm that LM incorporated into MPL-fabricated microstructures retains its biological activity and that LM-OSCMs support and enhance the attachment, spreading, and proliferation of living cells.

OSs have been one of the most promising materials in the emerging field of bioelectronics owing to their mechanical flexibility which simulates properties of biological tissue,

mixed ionic and electronic conduction that facilitates efficient biosignal transduction, and biocompatibility and facile functionalization with biomolecules for tuning biological responses.[65–68] Fabrication of organic bioelectronic devices have mostly relied on conventional lithography techniques involving photomask processes to fabricate metal electrical contacts and interconnects followed by OS electrochemical patterning[41–43], impaired with their challenges and limitations. Here, we propose a maskless method based on MPL for fabrication of bioelectronics, as schematically illustrated in Figures 5A–C. The proposed shape and geometry of the device is similar to Michigan style neural electrodes.[35] The MPL fabrication process begins with construction of insulating electrode shank and base (height: 2 μm) from the polymer resin (without added OS) (schematic illustration Figure 5A and optical micrograph representation Figure 5G). Next, the resin is replaced with the OS composite resin (OS concentration: 0.5 wt%) and OSCMs including electrode sites (height: 7 μm, diameters: 1, 5, 10, 20, 40, and 80 μm), interconnect cables (width: 1 μm, height: 2 μm), and contact pads (length: 20 μm, width: 20 μm, height: 7 μm) are fabricated (schematic illustration Figure 5B and optical micrograph representation Figure 5I). Finally, the insulating layer is fabricated from the polymer resin (without added OS) to encapsulate the interconnect cables (height: 3 μm) (schematic illustration Figure 5C and optical micrograph representation Figure 5J). It is worth noting that the fabrication process shown in Figure 5B can be further modified for the development of enzyme based-biosensors by first fabrication of electrode sites from OS composite resin containing biorecognition molecule such as glucose oxidase enzyme (GOx) (schematic illustration Figure 5D and optical micrograph representation Figure 5H), followed by construction of interconnect cables and contact pads from OS composite resin (without enzyme), (schematic illustration Figure 5E and optical micrograph representation Figure 5I), and finally fabrication of the insulating layer (schematic illustration Figure 5F and optical micrograph representation Figure 5J). Figures 5G–J represent optical micrographs of the fabrication steps, and Figures 5K and 5L show the SEM of MPL-fabricated microstructures.

Next, we measured and characterized the electrochemical properties of the OS composite microelectrode sites shown in the SEM micrographs in Figure 5K using electrochemical impedance spectroscopy (EIS) and cyclic voltammetry (CV). As shown in Figure 6A, the impedance magnitude decreased across all frequencies (1 to $10^5$ Hz) as the diameter of the OS composite microelectrode sites increased. The larger surface area resulted in higher double layer capacitance, which is inversely related to the impedance.[69] Specifically, at the biologically relevant frequency of ≈ 1 kHz, the impedance magnitude significantly decreased from 63.13 ± 4.56 kΩ to 19.28 ± 3.08 kΩ ($p$<0.001) as the diameter of sites increased from 1μm to 80 μm (Figure 6B). The trend of both impedance magnitude and phase angle of the OS composite sites (Figure 6C) were in agreement with previous studies of electrochemical patterned OS.[70–72] In particular, OS composite sites exhibited capacitive behavior at low frequencies (1-10 Hz) due to the dominance of double layer capacitance. However, at frequencies between 10 and $10^3$ Hz, OS composite sites became more resistive as the frequency increased because of predominance of charge transfer reaction and diffusion associated with mixed ionic and electronic conduction of the OS (Figure 6C).[71, 72]

It has been reported that pristine OS[73] structures and OS composite structures containing > 70 wt% OS[74, 75] could significantly swell in aqueous/ionic solutions. In agreement with these findings, here, adding 0.5 wt% OS did not cause a significant change in the water absorption of MPL- fabricated microstructures (Figure S10A, Supporting Information, no statistically significant difference between OS composite polymer and polymer) and the impedance was relatively stable in phosphate buffered saline during swelling (PBS, pH= 7.4, T= 37°C) (≈7% increase at biologically relevant frequency 1kHz after 3 days, Figure S10B, Supporting Information). In addition, the OS composite polymer exhibited less than ≈2.5% mass loss after 10 days (no statistically significant difference) of incubation in phosphate buffered saline (PBS, pH= 7.4, T= 37°C), presumably due to hydrolysis of ester bonds (Figure S10C, Supporting Information,). These results were in agreement with to those reported previously.[76, 77] CV was conducted to study redox reactions of the OS composite sites due to ion exchange between OS and electrolyte. As shown in Equation 1, the redox reaction is accompanied by the transportation of cations inside and outside of the OS:

$$\left[OS^{n+}(A^-)_n\right] + nC^+ \underset{-e^-}{\overset{+e^-}{\rightleftharpoons}} \left[OS^0(A^-)_n\left(C^+\right)_n\right] \quad \text{(Equation 1)}$$

, where $OS^+$ represents the oxidized state, $OS^0$ represents the neutral state, $A^-$ represents immobile charge balancing anions, and $C^+$ represents cations in the electrolyte. During CV, OS composite sites were swept between −0.8 V and 0.4 V at a constant scan rate of 0.1 V $s^{-1}$ and the cyclic I-V curves were obtained (Figure 6D). The anodic peak potential (oxidation) was $E_{pa}$ ≈ 0.1 V and cathodic peak potential (reduction) was $E_{pc}$ ≈ −0.2 V which were in the range of previously reported OS.[39, 71, 72] As shown in Figure 6D, the cathodic and anodic currents drastically increased as the surface area of the OS composite sites increased presumably due to increasing ion diffusion at the OS microelectrode-electrolyte interface. The charge storage capacity (CSC) is proportional to the surface area under the I-V curves and determines the charge of mobile carriers accumulated within the OS composite polymer during a I-V cycle (Equation S3, Supporting information). It is noteworthy that the charge storage capacity (Figure 6E) and specific capacitance (Equation S2 and Figure S11, Supporting Information) significantly increased from 2.38 ± 0.18 nC $\mu m^{-2}$ to 89.73 ± 15.14 nC $\mu m^{-2}$ and from 435 ± 19 F $g^{-1}$ to 16398 ± 1597 F $g^{-1}$, respectively ($p$<0.001).

To demonstrate the potential application of our MPL-based microstructures, we designed and fabricated a glucose biosensor as described and illustrated in Figures 5D–F. To date, the most commonly used amperometric glucose biosensors utilize enzyme glucose oxidase (GOx) for the specific recognition of glucose and the glucose concentration is determined by consumption of oxygen (to produce hydrogen peroxide) and oxidation of hydrogen peroxide at high potential ≈ + 0.7V. In this study, GOx was encapsulated within the solidified OS composite microelectrodes (GOx-OSCM) via the MPL process from a homogeneous resin containing 0.3 mM GOx and 0.5%wt OS (Figure S12A, Supporting Information, see resin preparations and amperometric response measurements in Experimental Section). EIS and CV plots of GOx-OSCM microelectrodes in the absence of glucose showed that the electroactivity of OS composite polymer was relatively affected by the incorporation of GOx, presumably due to excessive ion transportation that was caused

by the electronegative nature of GOx (Figures S12B and S12C, Supporting Information).[78] Figure 6F depicts CVs of GOx-OSCM microelectrodes in the presence of glucose at different concentrations. Further evaluation of CSC revealed a good level of stability as its electrochemical properties showed a slight reduction (≈3%) as the glucose concentration increased from 0.1 to 3mM. We evaluated the performance of the biosensor by measuring the currents at a pre-set polarization potential of + 0.3 V vs. Ag/AgCl upon injection of increasing glucose concentration from 0.1 mM to 3 mM (red curve, Figure 6G) in phosphate buffered saline (PBS, pH= 7.4, T= 37°C), a clinically relevant concentration range for glucose in cerebrospinal fluid[79] where the glucose concentration is two thirds that of its concentration in blood.[78]. Various attempts have shown that OSs could be used as mediators for amperometric detection of glucose at polarization potential lower than + 0.7 V (i.e. 0.3-0.4 V), presumably due to the electron pathway shown in Figure 6H, which is an oxygen-independent detection mechanism (see glucose detection in deoxygenated buffer solution and Figure S13, Supporting Information) .[80–82] As shown in Figure 6G, OS composite sites without encapsulated GOx (blue curve) did not show any current flow with increased glucose addition, demonstrating that the glucose detection was enzymatic. Figure 6I shows the amperometric response of the GOx-OSCM biosensor to successive addition of 0.2 mM glucose (1), 0.1 mM acetaminophen (2), 0.1 mM ibuprofen (3), 0.1 mM ascorbic acid (4), and 0.1 mM urea (5). The concentration of the latter interference species in blood is typically lower than glucose, however they can produce large amperometric current compared to the glucose presumably due to their faster charge transport speed.[83] While the current response of glucose for GOx-OSCM biosensor was remarkable at potential + 0.3 V, the biosensor exhibited trivial current response to other analytes (Figure 6I), which can be attributed to elimination of oxidation effect from electrochemically active interferences at low potential of + 0.3 V. These results underscore the specificity and anti-interference performance of the biosensor. The response curve of the biosensor showed an operating range of glucose concentration 0.1-3 mM (dynamic range of current response 0-2 μA), with a sensitivity of 232.9 ± 22.5 μA $mM^{-1}$ $cm^{-2}$ between 0.1 and 1 mM, a limit of detection of 0.03 mM (Figure 6J). In addition, the biosensor exhibited a response time of ≈ 4 s. The sensitivity of the MPL-fabricated GOx-OSCM microelectrodes marks a significant improvement compared to other GOx immobilization methods in the literature including physical binding, entrapment, and covalent attachment to electroactive materials[78, 84–99] that may suffer from inefficient enzyme loading and degradation of enzyme activity[100, 101] (Figure 6K, Table S4, Supporting Information). The method of immobilization of enzyme plays an important role in enzyme stability and retention of enzyme activity, thus affecting the overall performance of the biosensor.[101, 102] The efficient encapsulation of enzymes within organic and in-organic matrices for the development of biosensor with improved stability and high sensitivity has been reported .[101–107] Thus, the greater sensitivity may be attributed to the efficient GOx loading by direct encapsulation of the enzyme within MPL-fabricated OS microelectrodes (see preparation of GOx-OSCM and GOx-OS biosensors and amperometric measurements, Figures S14, Supporting Information). Furthermore, we do not anticipate any changes in GOx activity/stability when subjected to irradiation for ≈ 0.03 s by the femtosecond laser with peak power density of 141.54 $\times 10^6$ W $cm^{-2}$ (Equations S4–S9, Supporting Information). Previous studies reported that exposure times > 1h for femtosecond lasers with peak power density of $10^6$-$10^{12}$ W $cm^{-2}$ [108] could cause adverse

effects on the structure of DNA and proteins (damage and inactivation).[109–111] It has been reported that a femtosecond near infrared laser (peak power density ≈ $120 \times 10^6$ W $cm^{-2}$) with short exposure time (3-10 s) can be utilized for safe and efficient *in vivo* gene delivery and expression without any adverse effects such as apoptosis, DNA/protein degradation, and tissue damage.[112] We further investigated the reproducibility (i.e. precision) of the GOx-OSCM biosensor, which describes the closeness of agreement between current signals obtained using the same method but different GOx-OSCM biosensors. For 0.2 mM glucose injection, the mean value of the current measured by three different biosensors was 0.38 μA and the precision (relative standard deviation, RSD) was 4.02%. The Food and Drug Administration has stablished that for development of bioanalytical methods the determined precision should not exceed 15% of the RSD[113], therefore, the GOx-OSCM biosensor can be used to detect glucose with sufficient precision.

Finally, we evaluated the biocompatibility of the OS composite structures by culturing lymphocytes, namely splenic T-cells and B-cells, on the fabricated surfaces and compared them with control surfaces (without OS composite structures), with respect to viability and expression of activation markers of the cells by flow cytometry, after 7 days of culture. OS composite polymers did not induce cell mortality with approximately 94% cell viability compared to the control surfaces (no statistically significant difference) (Figure S15A, Supporting information). Potential effect of OS composite polymers on cell activation was also studied. Expression of CD69 (activation marker for T-cells) and CD86 (activation marker for B-cells) were analyzed by flow cytometry (Figure S15B and Figure S16, Supporting Information). After 7 days of culture, there was no significant difference in the expression of activation markers on the lymphocytes between OS composite structures and control surfaces. Together, these results demonstrate that a 7-day incubation of primary T-cells and B-cells with OS composite polymer did not induce cell mortality or cell activation. These findings support the biocompatibility of OSCMs with primary mammalian cells, allowing these cells to survive, without any untoward inhibitory or stimulatory effects, thus supporting their use in biomedical applications. Clearly, in vivo studies are warranted to further assess their biocompatibility.

In summary, this paper presents a homogeneous and transparent MPL compatible resin-doped with an OS to fabricate 3D OS composite microstructures with enhanced electrical conductivity. Using MPL process, we fabricated various microelectronic elements and devices on glass and PDMS substrates, including micro-resistors, micro-capacitors and μPCBs. We demonstrated that laminin can be incorporated into these OS composite polymers without a significant loss of activity as the resultant structures were able to support cellular adhesion and growth. Moreover, we extended the above-mentioned MPL process to fabricate enzyme-based biosensors, and as a proof-of-concept, incorporated GOx into the microstructures and demonstrated that glucose can be detected with high sensitivity, specificity, and reproducibility. We anticipate that the presented MPL-compatible OS composite resins will pave the path towards production of soft, bioactive, and conductive microstructures for various applications in the emerging fields of flexible bioelectronics/biosensors, nanoelectronics, organ-on-chips, and immune cell therapies.

## Experimental Section

### Materials:

Poly(ethylene glycol) diacrylate (PEGA, $M_n$=700), high conductivity grade of organic semiconductor poly(3,4-ethylenedioxythiophene)-poly(styrenesulfonate) 1.0 wt.% in $H_2O$, 3-(trimethoxysilyl)propyl methacrylate (T-POL), laminin from Engelbreth-Holm-Swarm murine sarcoma basement membrane (L2020), anti-laminin antibody produced in rabbit, bovine serum albumin (BSA) lyophilized powder (≥96%, agarose gel electrophoresis), RBC lysis buffer, D-(+)-glucose, Urea (ACS reagent, 99.0-100.5%), glucose oxidase (GOx, type X-S from Aspergillus niger) were all purchased from Sigma Aldrich. Dimethyl sulfoxide (DMSO, molecular biology grade), phosphate-buffered saline tablets (100 ml-biotechnology grade), ethanol (200 proof), and Sylgard™ 184 silicone elastomer (PDMS, Electron Microscopy Science) were ordered from VWR. Ethyl (2,4,6-trimethylbenzoyl) phenylphosphinate was purchased from Oakwood Chemical. Goat anti-rabbit IgG (H+L) Superclonal™ Secondary Antibody (Alexa Fluor 488) was purchased from ThermoFisher Scientific. Oregon Green 488 Phalloidin and DAPI were purchased from Invitrogen. FITC Anti-Mouse CD3 Antibody and PE Anti-Mouse CD69 Antibody were purchased from BiLegend. APC Cy7 Rat Anti-Mouse CD45R Antibody and FITC Rat Anti-Mouse CD86 Antibody were purchased from BD Biosciences. Acetaminophen, Ibuprofen, and Ascorbic acid were donated to the lab.

### Resin Preparations:

Composite resins contained DMSO (25 wt%), OS (0.1-0.5 wt%), and PEGDA (72.5 - 72.9 wt%). Non-conductive resins included neither PEDOT:PSS nor DMSO. In all formulations, liquid resins were composed of a constant amount of T-POL (2 wt%). These components were added sequentially: OS, DMSO, PEGA, and T-POL. The mixture was magnetically stirred for 2 hr, followed by 1 hr of degassing, using a desiccator. Functionalized ink was prepared by addition of laminin (LM, 100 μg $ml^{-1}$) or GOx (3.5 KU $ml^{-1}$) to the composite resin (containing 0.5 wt% OS) using a vortex mixer for 30 s.

### UV-VIS Spectroscopy:

Optical transparency of the resin was measured using a UV-VIS spectrometer (SpectraMax M5, Molecular Devices) and SoftMax Pro software (version 6.5). Resins with various OS concentrations were prepared and poured into cuvettes (PerkinElmer instruments). Transmittance was measured at wavelength spectrum of 350-750 nm. Air was used as the reference.

### PDMS Substrates:

A blend of 1:10 curing agent: PDMS base elastomer (mass ratio) was prepared and well mixed, followed by degassing for 1 hr. The mixture was then poured in a glass mold, spin-coated at a speed of 1000 rpm for 5 s, followed by heat treatment in an oven at 60°C for 2 hr. Thin, flexible PDMS films (thickness of 0.2 mm) were then detached from the glass.

### Fabrication of gold-coated substrates:

First, glass coverslips were partially masked by temperature-resistant tape, followed by electron beam evaporative deposition (Thermionics eBeam Evaporator, Thermionics) of a thin layer of chromium (10 nm) and gold (100 nm). Chrome acted as an intermediate layer to improve attachment of gold to glass.

### Surface Treatment of Substrates:

In order to facilitate the adhesion of 3D microstructures to PDMS film / glass coverslip, surface plasma oxidation and salinization treatment were performed prior to MPL fabrication. The substrates were first exposed to plasma (115 V, 50/60 Hz, 0.35 A) for 1 min, using a Handheld Corona Surface Treater (BD-20, Electro-Technic Products). Salinization solution was prepared by adding 100 μL of 3-(trimethoxysilyl) propyl methacrylate to 2 mL ethanol, and 6 ml diluted acetic acid (1:10 glacial acetic acid:water). 200 μL of this solution was added to the surface of substrates. After 5 min, excess solution was poured off, followed by a gentle rinse in ethanol to remove any residual reagent from the surface.

### Multiphoton Lithography:

A droplet of the resin (≈ 10 μl) was loaded between a glass slide and salinized PDMS film / coverslip which were attached to one another by double-sided tape supports. The specimen was positioned on the sample holder located on top of a piezostage (VP-5ZA, Newport), which was connected to XY-stages (XMS 160, Newport). A femtosecond laser (Mai Tai™ DeepSee, Spectra Physics), operating via Mai Tai™ software (version 2.0), was focused at the PDMS film / coverslip interface through a 40X objective with numerical aperture 0.65 (Plan N, FN 22, Olympus). The resin was crosslinked using 130 femtosecond laser irradiation at wavelength 800 nm, and laser power:17 mW through a Ti-sapphire oscillator operating at 80 MHz (Ti-sapphire laser, 130 fs, 80 MHz, 780 nm) and simultaneous 3D movement of the XYZ-stages, resulting in layer by layer construction of the 3D microstructure upside down on the PDMS film / coverslip. XYZ-stages were connected to a motion controller / driver (XPS, Newport) and their movement was adjusted by nFab software (version 5.0.14, Newport). Structures were designed using Autodesk® Fusion 360™ software and the sketches were converted into stereolithography format prior to being imported to nFab. Microstructures were fabricated at scanning rate of 50 μm $s^{-1}$ and after completion of the MPL process, PDMS film / coverslip was detached from the supports and immediately soaked in ethanol for 1 min to wash off the remaining unsolidified resin. The samples were soaked in ethanol for 2 hr to remove any excess compounds.

### Fourier Transform Infrared Spectroscopy:

A droplet of pure OS, composite resin (with OS), and polymer resin (without OS) was placed on a calcium fluoride microscope slide. Photosensitive resins were crosslinked using a long wave ultraviolet (UV) lamp (Black-Ray, model B 100 AP). Samples were characterized using FTIR imaging system (Agilent 670 spectrometer coupled to a Cary 620 microscopy system). Prior to imaging, a background scan was performed and FTIR images were acquired in transmission mode over 750 to 4000 $cm^{-1}$ spectral range.

### Conductivity, Resistance, and Capacitance Measurements:

Semiconductor Device Parameter Analyzer (B1500A, Keysight Technologies Inc) was used for electrical measurements. Briefly, probe tips (Signatone, diameter 1 μm) of two electrodes connected to Source Measurement Unit (SMU-8, Keysight Technologies Inc) were placed on two sides of the gold-coated coverslip. Probe movement was thoroughly adjusted using micromanipulators and a stereo microscope (Discovery. V8, ZEISS Germany). I-V sweep was performed by applying a voltage in the range of −3 V to 3 V (increasing step: 50 mV), and current was automatically recorded. EasyEXPERT group+ software (resident GUI-based, Keysight Technologies Inc.) was used to analyze the data. In the case of micro-printed circuit board (μPCB), probes touched both ends of cube-cylinder sites simultaneously, followed by I-V sweep. Resistance/conductance was derived from the slope of the I-V graph, and conductivity was calculated based on the geometry of the structure. For capacitance measurements, hysteresis loop was obtained for an array of 3 microcapacitors by performing double I-V curve in the range of −3 V to 3 V and a scan rate of 2 V $s^{-1}$.

### Surface Texture Measurements and Surface Roughness Analysis:

Surface texture measurements and roughness profile parameters of the MPL-fabricated microstructures were assessed using non-contact Material Confocal Microscopy LSM800 (Zeiss, Germany), an objective lens Epiplan-Aprochromat 100X, NA 0.95 DIC, and ConfoMap® software (Zeiss, Germany) in accordance with ISO 4287. Travel mechanism accurately moved with a resolution of 10 nm. Confocal laser scanning microscopy was performed for areal roughness measurements over the entire surface (50 μm × 50 μm), which expands the profile (line roughness) three dimensionally, generates better statistics, and produces stable results. The root mean square roughness (Rrms) parameter was reported.

### Electrochemical Impedance Spectroscopy (EIS) and Cyclic Voltammetry (CV):

Both measurements were conducted using Autolab PGSTAT 302N (Metrohm USA Inc.) and Nova Frequency Response Analyzer software (version 2.1, Metrohm USA Inc.) in potentiostatic mode. A solution of 0.1 M PBS (pH= 7.4) was used as the electrolyte. A three-electrode configuration including Ag/AgCl reference electrode, platinum foil counter electrode, and one end of the microstructure (fabricated on the coverslip) were immersed in the PBS solution, while the other end was connected to the working electrode outside of the electrolyte. In EIS, a sinusoidal AC signal with 10 mV rms amplitude was imposed to measure the impedance over a frequency range of 1-$10^5$ Hz. For CV staircase analysis, the potential of the working electrode was swept across −0.8 V to 0.4 V range with respect to the Ag/AgCl reference electrode at a constant scan rate of 0.1 V $s^{-1}$. In each experiment, CV was repeated three times and the third cycle was used to plot CV graphs.

### Immunohistochemistry (IHC):

In order to detect laminin on MPL-fabricated microstructures, IHC was performed in the following order: (1) 0.01 M of blocking agent solution (BSA diluted in 1X PBS) was added to the surface of substrate. After 30 min of incubation in room temperature, substrate was gently rinsed in deionized water (DIW); (2) primary anti-laminin antibody ( volume dilution ratio of 1:30 in 1X PBS) was added to the substrate and kept at temperature of 4°C

overnight; (3) Substrate was triple washed in DIW (each wash took 20 s); (4) A secondary antibody solution (volume dilution ratio of 1:100 in 1X PBS) was added to the substrate and was incubated for 60 min at room temperature without exposure to ambient light; (5) finally, the substrate was triple washed in DIW and it was ready for fluorescent imaging.

### Optical and Fluorescent Microscopy:

Optical micrographs were captured using an upright microscope (Imager Z1, Zeiss Germany). ZEN-pro Axiovision digital processing software (Zeiss Germany) was used to analyze the images. For fluorescent imaging, fluorescent-tagged laminin was detected using the UV light bulb (X-Cite, Series 120 Q, Lumen Dynamics) and ZEN-pro Axiovision was used to analyze the images and fluorescence quantification.

### Scanning Electron Microscopy (SEM):

Coverslips were mounted on aluminum stubs by double-sided carbon tape and were then sputtered with gold using desktop sputtering system (DESK-II, Denton Vacuum LLC) for 60 s at 40 mA to reduce charging effects. Scanning electron microscope (XL-30S FEG, FEI) was employed to capture images in secondary electron detection mode, at operation voltage of 5 kV. Adobe Photoshop was used to modify the brightness / contrast of the SEM images. SEM images were pseudo-colored red/green for better illustration of the MPL-fabricated OS composite polymer microstructures and polymer microstructures.

### Endothelial Cell Culture and Microscopy:

First, 5 by 5 array of connected cubes with dimensions of 100 μm × 100 μm × 2 μm (length × width × height) were 3D printed via MPL, providing a total area of 500 μm × 500 μm. The microstructures were fabricated using composite polymer resin with or without incorporated laminin. Following MPL fabrication, samples were soaked in ethanol for 2 hr to make sure DMSO is completely removed from the structure. Primary mouse endothelial cells were isolated from glomeruli of H-2K$^{b}$-tsA58 mice (Jax Stock # 032619) as previously described.[114] After trypsinization, $10^6$ cells were seeded onto a 60 mm dish containing a glass coverslip with MLP-microstructures. Cells were cultured for 48 hr and cell adherence was assayed by fixing the cells in 4% paraformaldehyde for 20 min followed by permeabilization using 0.1% Triton X-100 for 5 min; F-actin was stained using Oregon Green 488 phalloidin for 60 min. After washing in PBS, cell nuclei were DAPI stained, and coverslips were mounted on glass slides ZEN-pro Axiovision digital processing software was used to analyze the images and fluorescence quantification. Following imaging by epifluorescence microscopy, Adobe Photoshop was used to adjust image brightness/contrast.

### Degradation Studies:

Arrays of cylindrical OS composite polymers were fabricated and then were soaked in ethanol for 2 hr to remove any excess compounds. The initial mass ($W_0$) of the samples was recorded using a Mettler Toledo (XPR504S). The samples were then incubated at 37 °C in 1 mL of PBS (pH=7.4) for different amount of time until swelling ratio and mass loss analysis at the desired timepoint. At the designated time points, swollen samples (n=5) were removed from the PBS and then rubbed gently with a Kimwipe to remove any excess water.

The samples then were weighed to measure the swollen mass ($W_w$). The samples were then dried in a vacuum oven and were weighed again ($W_d$). The mass loss and the swelling ratio percentages of the samples were calculated with the following equations:

$$Mass\ loss\ \% = \frac{(W_0 - W_d)}{W_0} \times 100$$

$$Swelling\ ratio\ \% = \frac{(W_w - W_d)}{W_d} \times 100$$

## Amperometric Response Measurements:

BioStat™ (ESA Biosciences, Inc.) was used to record the current response at polarization potential of +0.3 V vs. Ag/AgCl, which was applied to the biosensor in a stirred solution of 20 ml PBS (1X, pH= 7.4, T=37°C). Once the background current was stabilized, successive injections of glucose solution were added (cumulative concentration ranging from 0.1 mM to 3 mM). The size of MPL-fabricated GOx-OSCM composite electrode was 675 μm × 675 μm × 2 μm (length × width × height). In the three-cell configuration, a Pt wire counter electrode and an Ag/AgCl reference electrode were used. Resulting current measurements were used to calculate the sensitivity and limit of detection (LOD) of the biosensor. The reproducibility of the biosensors was investigated by measuring the current generated by 0.2 mM glucose in 20 ml PBS by using three different glucose biosensors. Each biosensor was tested by three replicates of analysis. The total mean value was calculated, and the relative standard deviation (RSD) provided the analytical precision. The RSD was calculated using the following equation:

$$RSD\ (\%) = \frac{Standard\ deviation}{Average} \times 100 \quad \text{(Equation 2)}$$

## Spleen Cell Culture and Flow Cytometry:

Spleen cells were isolated from 3-month-old C57/B6 mice. Briefly, spleen was dissected and minced through a 70-micron sieve and red blood cells were lysed using RBC lysis buffer. After washing and counting cells using Cellometer (Nexcelom Bioscience), spleen cells were cultured in RPMI 1640 media with 10% fetal bovine serum either without (control) or with exposure to OS composite polymer. After 7 days of exposure, the immune cell numbers were counted and analyzed by flow cytometry using the following antibodies, FITC Anti-Mouse CD3 Antibody and PE Anti-Mouse CD69 Antibody, APC Cy7 Rat Anti-Mouse CD45R Antibody, and FITC Rat Anti-Mouse CD86 Antibody.

## Statistical Analysis:

Statistical analysis was carried out using OriginPro software (Northampton, MA). *P*-values are calculated by one-way ANOVA followed by Tukey Post-Hoc test. Data are presented as mean ± standard error of mean (SEM) and/or mean ± standard deviattion (SD). Symbols

** and *** represent significance level of $p<0.05$ and $p<0.001$, respectively and n.s. for not significance.

## Supplementary Material

Refer to Web version on PubMed Central for supplementary material.

## Acknowledgements

Funding was provided by the National Institute of Health, National Institute of Neurological Disorders and Stroke R01 NS087224, National Institute of Health R01 AR074096, and National Science Foundation CAREER Award DMR 1753328. Authors would like to thank Dr. David Mayerich from department of electrical and computer engineering at the University of Houston for providing FTIR imaging and. The authors also would like to thank Dr. Tommaso Baldacchini for his comments on MPL fabrication, and John Carter and William Clench from Newport Corporation for their technical assistance with laser and nFab software. In addition, the authors would like to thank Zeiss division of Confocal Microscopy for Advanced Imaging and Surface Topography for their technical assistance with surface roughness characterization using LSM 800 Materials and Dr. Long Chang at University of Houston nanofabrication Facility for his consultation and assistant with AFM.

## References:

[1]. Karnaushenko D, Kong T, Bandari VK, Zhu F, Schmidt OG, Adv. Mater 2020, 32, 1902994.

[2]. Jayne RK, Stark TJ, Reeves JB, Bishop DJ, White AE, Adv. Mater. Technol 2018, 3, 1700293.

[3]. Melzer JE, McLeod E, Nanophotonics 2020, 9, 1373.

[4]. Dong RH, Liu Y, Mou L, Deng JQ, Jiang XY, Adv. Mater 2019, 31, 1805033.

[5]. Matai I, Kaur G, Seyedsalehi A, McClinton A, Laurencin CT, Biomaterials 2020, 226, 119536. [PubMed: 31648135]

[6]. Chen KS, Lin IK, Ko FH, J. Micromech. Microeng 2005, 15, 1894.

[7]. Mu QY, Wang L, Dunn CK, Kuang X, Duan F, Zhang Z, Qi HJ, Wang TJ, Addit. Manuf 2017, 18, 74.

[8]. Tang Q, Shi SQ, Huang HT, Zhou LM, Superlattices Microstruct 2004, 36, 21.

[9]. Credi C, Fiorese A, Tironi M, Bernasconi R, Magagnin L, Levi M, Turri S, ACS Appl. Mater. Interfaces 2016, 8, 26332. [PubMed: 27610704]

[10]. Jeon S, Park JU, Cirelli R, Yang S, Heitzman CE, Braun PV, Kenis PJA, Rogers JA, PNAS 2004, 101, 12428. [PubMed: 15314211]

[11]. Li LJ, Fourkas JT, Mater. Today 2007, 10, 30.

[12]. Sugioka K, Nanophotonics 2017, 6, 393.

[13]. Jeon S, Malyarchuk V, Rogers JA, Wiederrecht GP, Opt. Express 2006, 14, 2300. [PubMed: 19503567]

[14]. Li LJ, Gattass RR, Gershgoren E, Hwang H, Fourkas JT, Science 2009, 324, 910. [PubMed: 19359543]

[15]. Sun ZB, Dong XZ, Chen WQ, Nakanishi S, Duan XM, Kawata S, Adv. Mater 2008, 20, 914.

[16]. Xia H, Wang JA, Tian Y, Chen QD, Du XB, Zhang YL, He Y, Sun HB, Adv. Mater 2010, 22, 3204. [PubMed: 20603886]

[17]. Blasco E, Muller J, Muller P, Trouillet V, Schon M, Scherer T, Barner-Kowollik C, Wegener M, Adv. Mater 2016, 28, 3592. [PubMed: 26953811]

[18]. Acharya S, Hill JP, Ariga K, Adv. Mater 2009, 21, 2959.

[19]. Liu LP, Yang D, Wan WP, Yang H, Gong QH, Li Y, Nanophotonics 2019, 8, 1087.

[20]. Liu Y, Xiong W, Li DW, Lu Y, Huang X, Liu H, Fan LS, Jiang L, Silvain JF, Lu YF, Int. J. Extreme Manuf 2019, 1, 025001.

[21]. Shukla S, Vidal X, Furlani EP, Swihart MT, Kim KT, Yoon YK, Urbas A, Prasad PN, Acs Nano 2011, 5, 1947. [PubMed: 21366284]

[22]. Nakamura R, Kinashi K, Sakai W, Tsutsumi N, Physical Chemistry Chemical Physics 2016, 18, 17024. [PubMed: 27297943]

[23]. Staudinger U, Zyla G, Krause B, Janke A, Fischer D, Esen C, Voit B, Ostendorf A, Microelectron. Eng 2017, 179, 48.

[24]. Xiong W, Liu Y, Jiang LJ, Zhou YS, Li DW, Jiang L, Silvain JF, Lu YF, Adv. Mater 2016, 28, 2002. [PubMed: 26754028]

[25]. Guo QC, Xiao SZ, Aumann A, Jaeger M, Chakif M, Ghadiri R, Esen C, Ma MY, Ostendorf A, J. Laser Micro Nanoeng 2012, 7, 44.

[26]. Oubaha M, Kavanagh A, Gorin A, Bickauskaite G, Byrne R, Farsari M, Winfield R, Diamond D, McDonagh C, Copperwhite R, J. Mater. Chem 2012, 22, 10552.

[27]. Restaino M, Eckman N, Alsharhan AT, Lamont AC, Anderson J, Weinstein D, Hall A, Sochol RD, Adv. Mater. Technol 2021, 6, 2100222.

[28]. Shirakawa H, Angew. Chem. Int. Ed 2001, 40, 2575.

[29]. Fahlman M, Fabiano S, Gueskine V, Simon D, Berggren M, Crispin X, Nat. Rev. Mater 2019, 4, 627.

[30]. Jastrzebska-Perfect P, Spyropoulos GD, Cea C, Zhao ZF, Rauhala OJ, Viswanathan A, Sheth SA, Gelinas JN, Khodagholy D, Sci. Adv 2020, 6.

[31]. Burroughes JH, Bradley DDC, Brown AR, Marks RN, Mackay K, Friend RH, Burn PL, Holmes AB, Nature 1990, 347, 539.

[32]. Zhan XW, Zhu DB, Polym. Chem 2010, 1, 409.

[33]. Hamedi M, Herlogsson L, Crispin X, Marcilla R, Berggren M, Inganas O, Adv. Mater 2009, 21, 573. [PubMed: 21161984]

[34]. Hamedi M, Forchheimer R, Inganas O, Nat. Mater 2007, 6, 357. [PubMed: 17406663]

[35]. Abidian MR, Ludwig KA, Marzullo TC, Martin DC, Kipke DR, Adv. Mater 2009, 21, 3764. [PubMed: 26345408]

[36]. Khodagholy D, Gelinas JN, Zhao ZF, Yeh M, Long M, Greenlee JD, Doyle W, Devinsky O, Buzsaki G, Sci. Adv 2016, 2, 1601027.

[37]. Cea C, Spyropoulos GD, Jastrzebska-Perfect P, Ferrero JJ, Gelinas JN, Khodagholy D, Nat. Mater 2020, 19, 679. [PubMed: 32203456]

[38]. Boehler C, Aqrawe Z, Asplund M, Bioelectron. Med 2019, 2, 89.

[39]. Groenendaal BL, Jonas F, Freitag D, Pielartzik H, Reynolds JR, Adv. Mater 2000, 12, 481.

[40]. Abidian MR, Kim DH, Martin DC, Adv. Mater 2006, 18, 405. [PubMed: 21552389]

[41]. Khodagholy D, Gelinas JN, Thesen T, Doyle W, Devinsky O, Malliaras GG, Buzsaki G, Nat. Neurosci 2015, 18, 310. [PubMed: 25531570]

[42]. Park S, Yang G, Madduri N, Abidian MR, Majd S, Adv. Mater 2014, 26, 2782. [PubMed: 24623531]

[43]. Asplund M, Nyberg T, Inganas O, Polym. Chem 2010, 1, 1374.

[44]. Cho YH, Park YG, Kim S, Park JU, Adv. Mater 2021, 33, 1.

[45]. Wang Y, Zhu CX, Pfattner R, Yan HP, Jin LH, Chen SC, Molina-Lopez F, Lissel F, Liu J, Rabiah NI, Chen Z, Chung JW, Linder C, Toney MF, Murmann B, Bao Z, Sci. Adv 2017, 3, 1.

[46]. Hong K, Kim YH, Kim SH, Xie W, Xu WCD, Kim CH, Frisbie CD, Adv. Mater 2014, 26, 7032. [PubMed: 24975133]

[47]. Yuk H, Lu BY, Lin S, Qu K, Xu JK, Luo JH, Zhao XH, Nat. Commun 2020, 11, 1. [PubMed: 31911652]

[48]. Zhu CX, Chortos A, Wang Y, Pfattner R, Lei T, Hinckley AC, Pochorovski I, Yan XZ, To JWF, Oh JY, Tok JBH, Bao ZA, Murmann B, Nat. Electron 2018, 1, 183.

[49]. Wang SH, Xu J, Wang WC, Wang GJN, Rastak R, Molina-Lopez F, Chung JW, Niu SM, Feig VR, Lopez J, Lei T, Kwon SK, Kim Y, Foudeh AM, Ehrlich A, Gasperini A, Yun Y, Murmann B, Tok JBH, Bao ZA, Nature 2018, 555, 83. [PubMed: 29466334]

[50]. Mendonca CR, Correa DS, Baldacchini T, Tayalia P, Mazur E, Appl. Phys. A: Mater. Sci. Process 2008, 90, 633.

[51]. Oesterreicher A, Roth M, Hennen D, Mostegel FH, Edler M, Kappaun S, Griesser T, Eur. Polym. J 2017, 88, 393.

[52]. Dong JJ, Portale G, Adv. Mater. Interfaces 2020, 7, 2000641.

[53]. Kim JY, Jung JH, Lee DE, Joo J, Synth. Met 2002, 126, 311.

[54]. Wang Y, Yang L, Shi XL, Shi X, Chen LD, Dargusch MS, Zou J, Chen ZG, Adv. Mater 2019, 31.

[55]. Kim YH, Sachse C, Machala ML, May C, Muller-Meskamp L, Leo K, Adv. Funct. Mater 2011, 21, 1076.

[56]. Zhang FL, Nyberg T, Inganas O, Nano Lett 2002, 2, 1373.

[57]. Ouyang BY, Chi CW, Chen FC, Xi QF, Yang Y, Adv. Funct. Mater 2005, 15, 203.

[58]. Stellacci F, Bauer CA, Meyer-Friedrichsen T, Wenseleers W, Alain V, Kuebler SM, Pond SJK, Zhang YD, Marder SR, Perry JW, Adv. Mater 2002, 14, 194.

[59]. Maruo S, Saeki T, Opt. Express 2008, 16, 1174. [PubMed: 18542191]

[60]. Kurselis K, Kiyan R, Bagratashvili VN, Popov VK, Chichkov BN, Opt. Express 2013, 21, 31029. [PubMed: 24514677]

[61]. Tao YF, Wei CYR, Liu JW, Deng CS, Cai S, Xiong W, Nanoscale 2019, 11, 9176. [PubMed: 31038144]

[62]. Tao YF, Fan XH, Xiong W, Liu JW, Deng CS, Long J, “Carbon nanotube-doped electric hydrogels via ultrafast laser processing and loading conductive polymer”, presented at 14th National Conference on Laser Technology and Optoelectronics (LTO), Shanghai, PEOPLES R CHINA, Mar 17-20, 2019.

[63]. Stromblad S, Cheresh DA, Trends Cell Biol 1996, 6, 462. [PubMed: 15157503]

[64]. Dadras-Toussi O, Khorrami M, Majd S, Abidian MR, Ieee, “Gradients of Surface-Bound Laminin on Conducting Polymer Films for Potential Nerve Regeneration”, presented at 10th International IEEE-EMBS Conference on Neural Engineering (NER), Prague, ELECTR NETWORK, May 04-06, 2021.

[65]. Malliaras G, Abidian MR, Adv. Mater 2015, 27, 7492. [PubMed: 26636956]

[66]. Hamedi M, Tvinstedt K, Karlsson RH, Asberg P, Inganas O, Nano Lett 2009, 9, 631. [PubMed: 19140695]

[67]. Kleber C, Lienkamp K, Ruhe J, Asplund M, Advanced Healthcare Materials 2019, 8, 1.

[68]. Muller C, Ouyang LQ, Lund A, Moth-Poulsen K, Hamedi MM, Adv. Mater 2019, 31, 1.

[69]. Kovacs G, in Introduction to the theory, design, and modeling of thin-film microelectrodes for neural interfaces, (Eds: Stenger D, McKenna TM), Academic Press, London, UK 1994, 121.

[70]. Cui XY, Hetke JF, Wiler JA, Anderson DJ, Martin DC, Sens. Actuat. A-Phys 2001, 93, 8.

[71]. Abidian MR, Martin DC, Biomaterials 2008, 29, 1273. [PubMed: 18093644]

[72]. Antensteiner M, Khorrami M, Fallahianbijan F, Borhan A, Abidian MR, Adv. Mater 2017, 29, 1702576.

[73]. Zhang SM, Cicoira F, Adv. Mater 2017, 29, 1.

[74]. Ghosh S, Inganas O, Adv. Mater 1999, 11, 1214.

[75]. Li Y, Li XD, Zhang SM, Liu L, Hamad N, Bobbara SR, Pasini D, Cicoira F, Adv. Funct. Mater 2020, 30, 1.

[76]. Stillman Z, Jarai BM, Raman N, Patel P, Fromen CA, Polym. Chem 2020, 11, 568. [PubMed: 33224282]

[77]. Zustiak SP, Leach JB, Biomacromolecules 2010, 11, 1348. [PubMed: 20355705]

[78]. Yang G, Kampstra KL, Abidian MR, Adv. Mater 2014, 26, 4954. [PubMed: 24719293]

[79]. Leen WG, Willemsen MA, Wevers RA, Verbeek MM, Plos One 2012, 7, 42745.

[80]. Kros A, Nolte RJM, Sommerdijk N, Adv. Mater 2002, 14, 1779.

[81]. Gerard M, Chaubey A, Malhotra BD, Biosens. Bioelectron 2002, 17, 345. [PubMed: 11888724]

[82]. Layton KN, Abidian MR, Ieee, “Conducting Polymer Nanofiber-Based Biosensor for Detection of Neurochemicals”, presented at 5th International IEEE Engineering-in-Medicine-and-Biology-Society (EMBS) Conference on Neural Engineering (NER), Cancun, MEXICO, Apr 27-May 01, 2011.

[83]. Jung S-H, Lee Y-K, Son Y-K, Technology, Journal of Electrochemical Science 2011, 2, 124.

[84]. Macaya DJ, Nikolou M, Takamatsu S, Mabeck JT, Owens RM, Malliaras GG, Sens. Actuat. B-Chem 2007, 123, 374.

[85]. Kros A, van Hovell WFM, Sommerdijk N, Nolte RJM, Adv. Mater 2001, 13, 1555.

[86]. Nien PC, Tung TS, Ho KC, Electroanalysis 2006, 18, 1408.

[87]. Piro B, Dang LA, Pham MC, Fabiano S, Tran-Minh C, J. Electroanal. Chem 2001, 512, 101.

[88]. Senel M, Nergiz C, Curr. Appl. Phys 2012, 12, 1118.

[89]. Chen YS, Huang JH, Chuang CC, Carbon 2009, 47, 3106.

[90]. Li J, Wang YB, Qiu JD, Sun D, Xia XH, Anal. Bioanal. Chem 2005, 383, 918. [PubMed: 16228200]

[91]. Liu XQ, Shi LH, Niu WX, Li HJ, Xu GB, Biosens. Bioelectron 2008, 23, 1887. [PubMed: 18387291]

[92]. Setti L, Fraleoni-Morgera A, Ballarin B, Filippini A, Frascaro D, Piana C, Biosens. Bioelectron 2005, 20, 2019. [PubMed: 15741071]

[93]. Tang H, Chen JH, Yao SZ, Nie LH, Deng GH, Kuang YF, Anal. Biochem 2004, 331, 89. [PubMed: 15246000]

[94]. Jung S-H, Lee Y-K, Son Y-K, J. Electrochem. Sci. Technol 2011, 2, 124.

[95]. Zhang SX, Wang N, Yu HJ, Niu YM, Sun CQ, Bioelectrochemistry 2005, 67, 15. [PubMed: 15967397]

[96]. Xue MH, Xu Q, Zhou M, Zhu JJ, Electrochem. Commun 2006, 8, 1468.

[97]. Yang WW, Wang JX, Zhao S, Sun YY, Sun CQ, Electrochem. Commun 2006, 8, 665.

[98]. Sun Y, Bai Y, Yang W, Sun C, Electrochim. Acta 2007, 52, 7352.

[99]. Christwardana M, Ji J, Chung Y, Kwon Y, Korean J Chem. Eng 2017, 34, 2916.

[100]. Homaei AA, Sariri R, Vianello F, Stevanato R, J. Chem. Biol 2013, 6, 185. [PubMed: 24432134]

[101]. Sheldon RA, Adv. Synth. Catal 2007, 349, 1289.

[102]. Park BW, Yoon DY, Kim DS, Biosens. Bioelectron 2010, 26, 1. [PubMed: 20554194]

[103]. Soares CMF, Dos Santos OA, De Castro HF, De Moraes FF, Zanin GM, Appl. Biochem. Biotechnol 2004, 113, 307. [PubMed: 15054215]

[104]. Pierre AC, Biocatal. Biotransform 2004, 22, 145.

[105]. Pauliukaite R, Ghica ME, Barsan M, Brett CMA, J. Solid State Electrochem 2007, 11, 899.

[106]. Rassas I, Braiek M, Bonhomme A, Bessueille F, Raffin G, Majdoub H, Jaffrezic-Renault N, Sensors 2019, 19.

[107]. Olea D, Viratelle O, Faure C, Biosens. Bioelectron 2008, 23, 788. [PubMed: 17931850]

[108]. Wigle JC, Holwitt EA, Estlack LE, Noojin GD, Saunders KE, Yakovlev VV, Rockwell BA, J. Biomed. Opt 2014, 19, 015008.

[109]. Lu CH, Lin KH, Hsu YY, Tsen KT, Kuan YS, J. Phys. D: Appl. Phys 2014, 47, 315402.

[110]. Botchway S, Reynolds P, Parker A, O'Neill P, Mutat. Res. Rev. Mutat. Res 2010, 704, 38.

[111]. Tsen KT, Tsen SWD, Sankey OF, Kiang JG, J. Phys. Condens. Matter 2007, 19, 472201.

[112]. Zeira E, Manevitch A, Khatchatouriants A, Pappo O, Hyam E, Darash-Yahana M, Tavor E, Honigman A, Lewis A, Galun E, Mol. Ther 2003, 8, 342. [PubMed: 12907157]

[113]. Tiwari G, Tiwari R, Pharm. Methods 2010, 2, 25.

[114]. Rops AL, van der Vlag J, Jacobs CW, Dijkman HB, Lensen JF, Wijnhoven TJ, van den Heuvel LP, van Kuppevelt TH, Berden JH, Kidney Int. 2004, 66, 2193. [PubMed: 15569308]

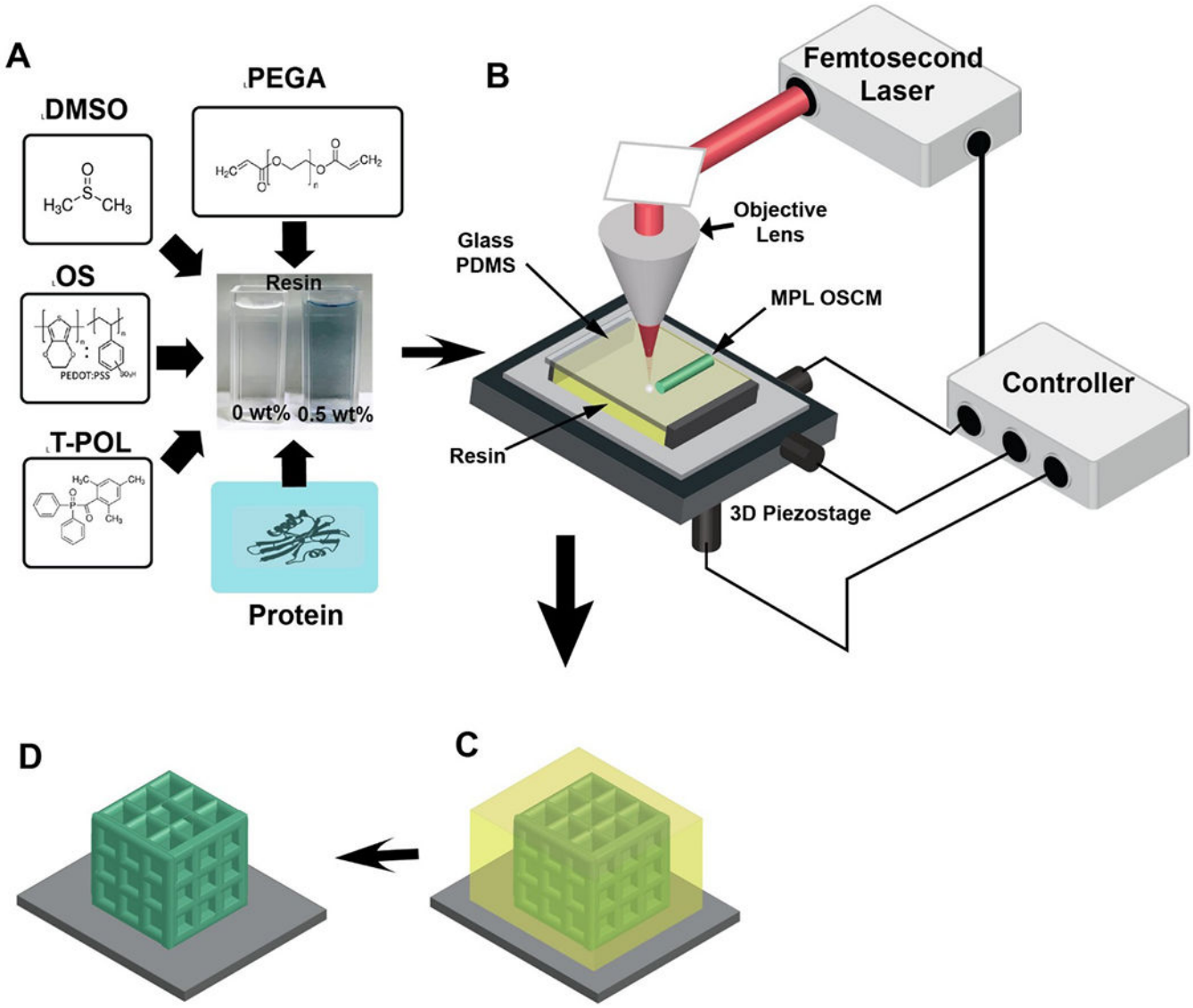


**Figure 1.**

Resin components and MPL fabrication process. A) Components of the OS composite resin: photopolymer poly(ethylene glycol) diacrylate (PEGA), organic semiconductor (OS) poly(3,4-ethylenedioxythiophene):poly(styrenesulfonate) (PEDOT:PSS), photoinitiator 3-(trimethoxysilyl)propyl methacrylate (T-POL), miscible agent dimethyl sulfoxide (DMSO) and proteins such as laminin and glucose oxidase. B) Experimental setup for the MPL process, including resin, glass/PDMS substrates, 3D piezostage, controller, femtosecond (fs) laser, and the objective lens. C) The OS composite resin (yellow color) is crosslinked by a focused fs laser to create 3D OSCMs (green color). D) The sample is then rinsed in ethanol to remove any unsolidified resin, leaving the 3D OSCMs on the substrate.

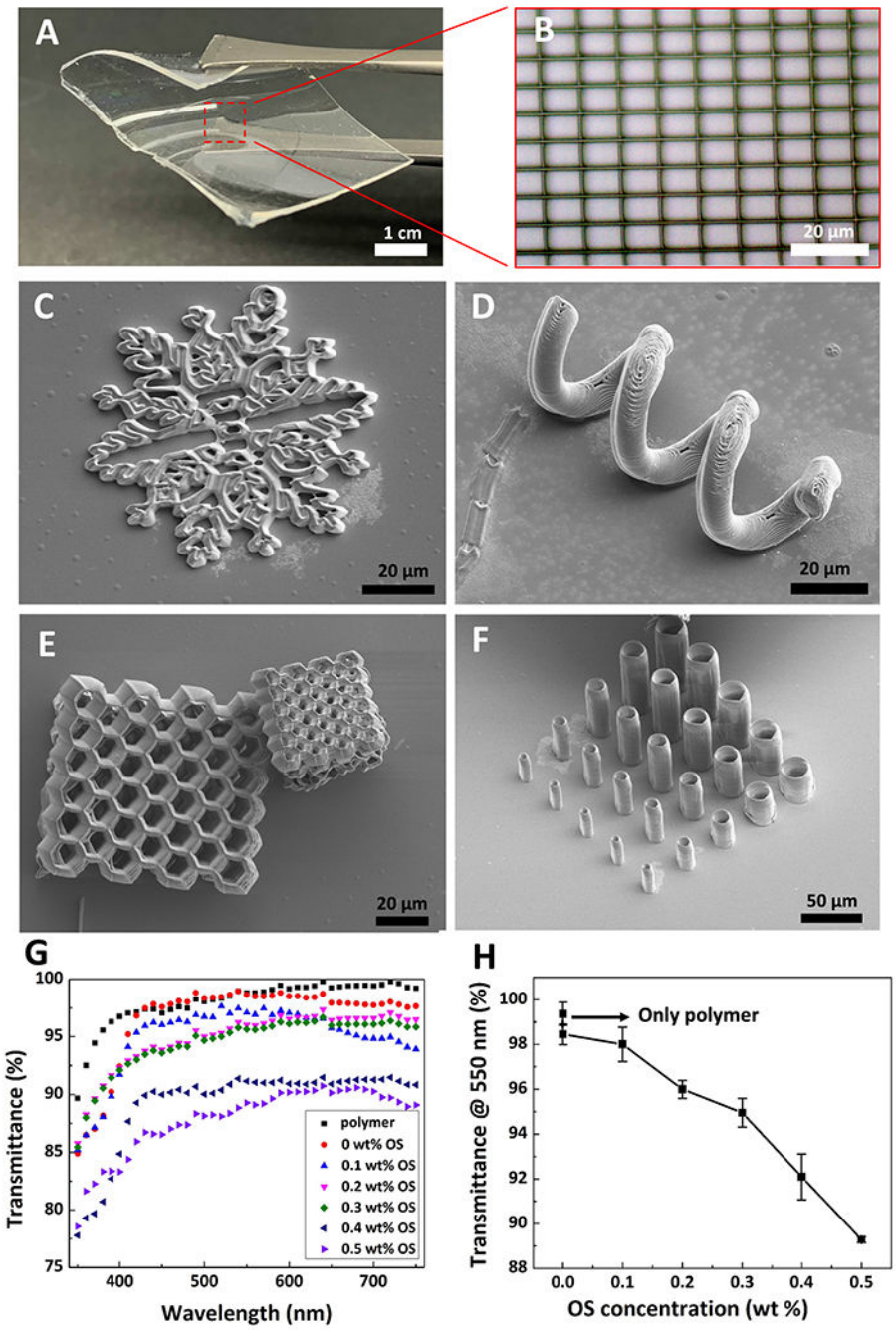


**Figure 2.**

3D microfabrication of conductive and bioactive microstructures based on OS composite resin via MPL and resin transparency. A) Thin and flexible PDMS substrate used for MPL fabrication. B) Optical microscopy micrograph of a micro-grid fabricated on PDMS film shown in (A). C-F) Scanning electron microscopy (SEM) micrographs of various microstructures, including a micro-snowflake (C), micro-spring (D), micro-honeycomb (E), and vertical micro-tubes (F). G) Optical transparency of the resin with various OS concentrations in the 350-750 nm wavelength spectrum. Black squares, red circles, blue

up-sided triangles, magenta down-sided triangles, green diamonds, dark blue left-sided triangles, and royal righ-sided triangles represent polymer (resin without DMSO), 0 wt% OS, 0.1 wt% OS, 0.2 wt% OS, 0.3 wt% OS, 0.4 wt% OS, and 0.5 wt% OS, respectively. H) Transmittance of resins at 550 nm with respect to various OS concentrations. Data shown as mean ± SEM, n=3

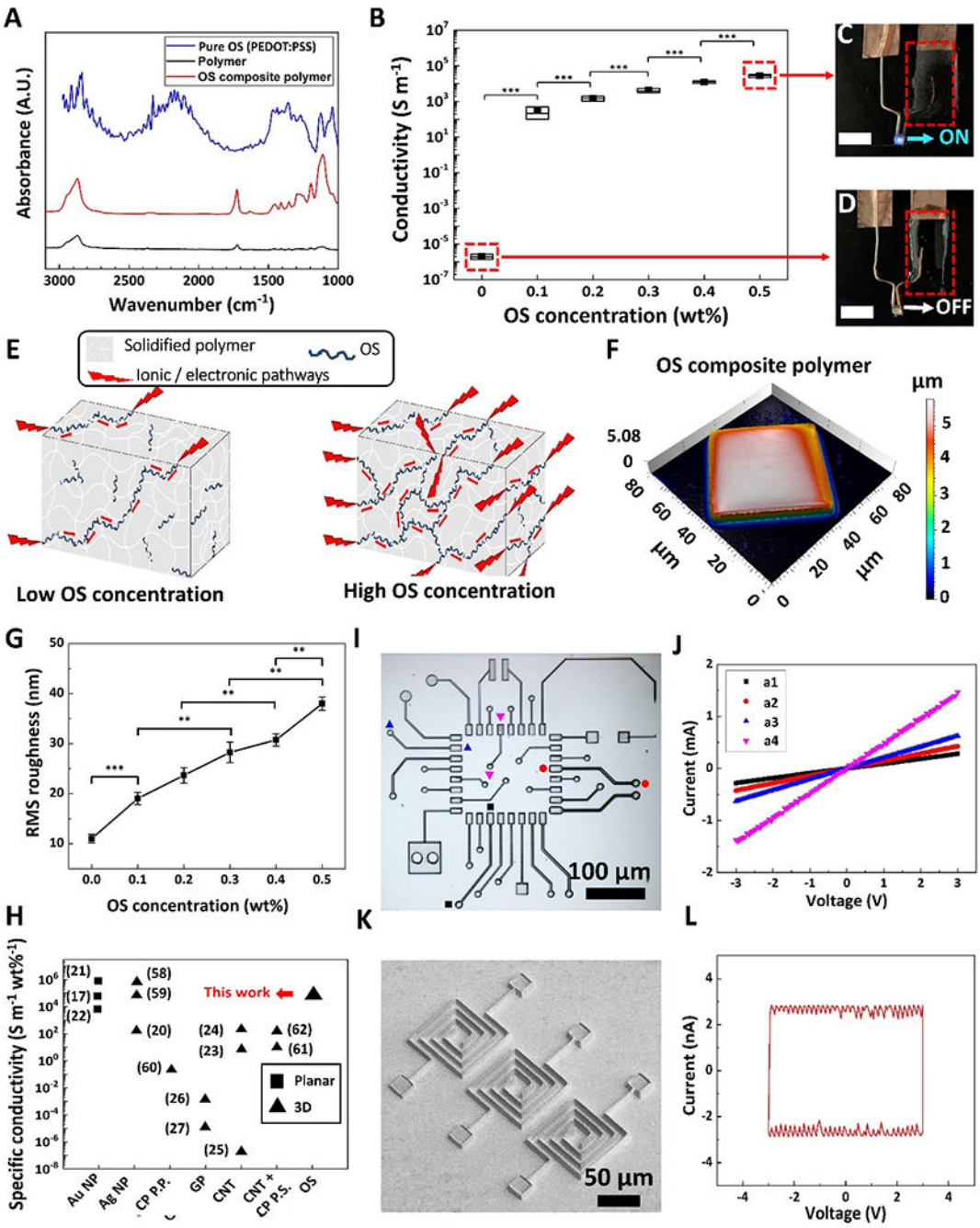


**Figure 3.**

Chemical, electrical, and physical characterization of MPL-fabricated microstructures. A) FTIR spectra of pure OS (blue curve), OS composite polymer (red curve) and polymer (black curve) microstructures. B) Electrical conductivity of OSCMs with respect to OS concentration in the resin. Data shown as mean ± SD, n = 9, *** $p<0.001$. In the box graph, black squares, horizontal lines and box range demonstrate mean, median, and SD, respectively. C and D) OS composite polymer structures (C) and polymer structures (D) acting as interconnects to drive a LED, respectively (scale bars: 5 mm). E) Schematic

of proposed conductivity of MPL-fabricated OS composite polymers. F) 3D view of color-coded height maps of cubic microstructures fabricated using OS composite resin (0.5 wt% OS), showing surface texture of MPL-fabricated microcubes. G) Surface roughness (Rrms) with respect to OS concentration. Data shown as mean ± SEM, n = 4, ** $p<0.05$, *** $p<0.001$. H) Comparison between specific conductivity of MPL-fabricated conductive microstructures in this study using OS composite resin and prior works using other conductive nanomaterials and post processing methods (Au NP: gold nanoparticles, Ag NP: silver nanoparticles, CP P.P.: conducting polymer (CP) post-polymerization (P. P.) after MPL fabrication, GP: Graphene, CNT: carbon nanotubes, CNT + CP P.S. : Doping CNT in resin, followed by post soaking of MPL-fabricated structures in CP solution, OS: organic semiconductor). Black squares represent planar structures, black triangles represent 3D microstructures. I) Optical microscopy micrograph of a μPCB comprised of various electrical elements. J) I-V graph of elements in μPCB: a1 (black squares), a2 (red circles), a3 (blue up-sided triangles), and a4 (magenta down-sided triangles); the straight lines indicate the resistor behavior of the elements. K) SEM micrograph of a microcapacitor array. L) Hysteresis loop of three microcapacitors in parallel. The rectangular-shaped I-V indicates capacitor behavior.

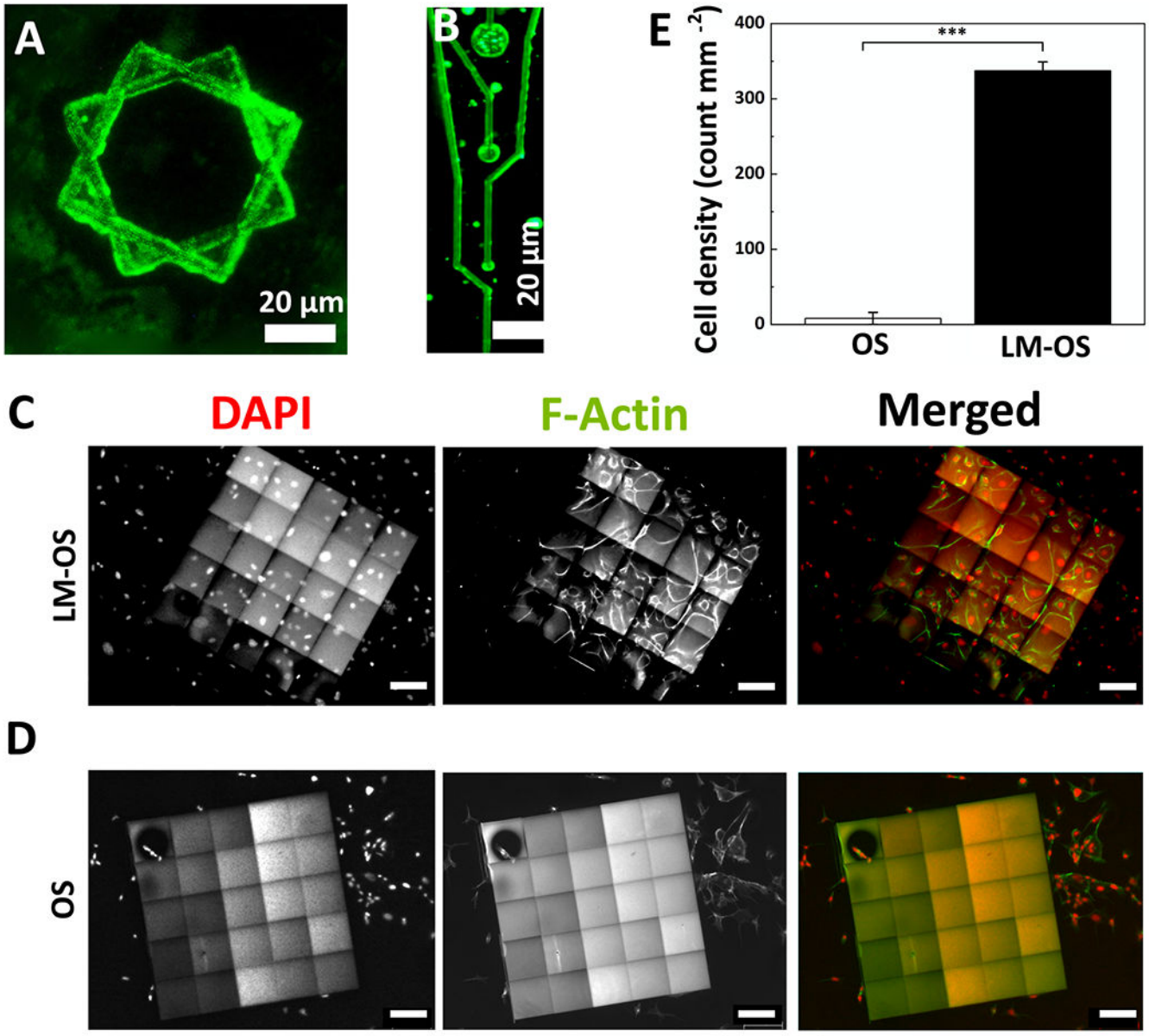


**Figure 4.**

Incorporation of laminin (LM) into MPL-fabricated OSCMs. A and B) Fluorescent microscopy micrographs of LM-OSCMs showing the incorporation and distribution of LM. C and D) Representative epifluorescence micrographs of endothelial cells fixed and stained with Oregon Green 488 phalloidin (green) and DAPI (red) to visualize F-actin and cell nuclei, respectively after 48 hr cultured on LM-OS microstructures (C) and OS microstructures (without LM) (D) (scale bars: 100 µm). E) Quantification of (C) and (D) showing the cell density, data shown as mean ± SEM, n = 3, *** $p$<0.001.

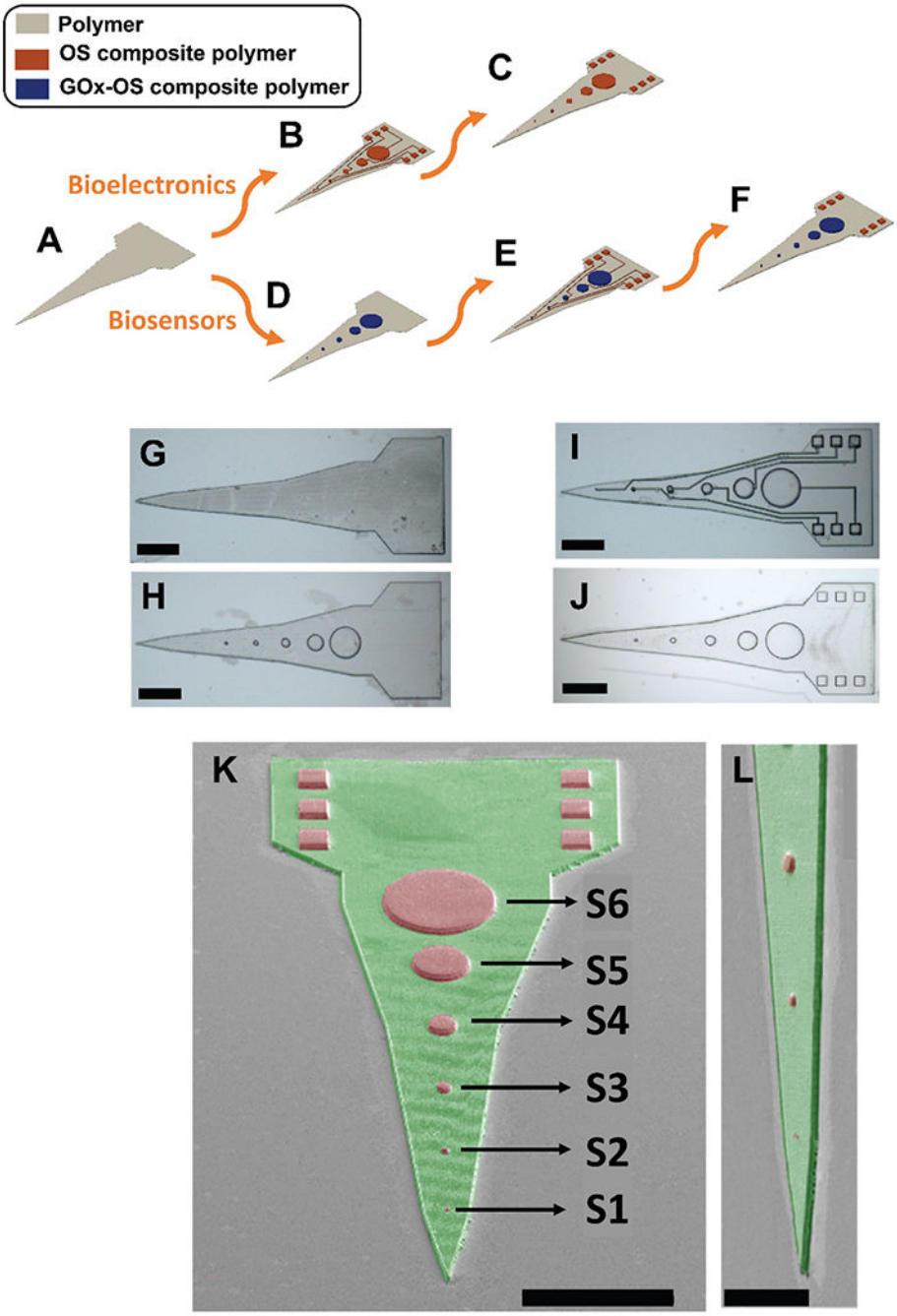


**Figure 5.**

MPL-based Fabrication process of hybrid Michigan-style microelectrode for bioelectronics and biosensors applications. A-C) Schematic illustrations for fabrication of bioelectronics: A) Construction of insulating electrode shank and base (height: 2 μm) using the polymer resin (without added OS). B) OSCMs including electrode sites (height: 7 μm, diameters: 1, 5, 10, 20, 40, and 80 μm), interconnect cables (width: 1 μm, height: 2 μm), and contact pads (length: 20 μm, width: 20 μm, height: 7 μm) were fabricated using the OS composite resin (OS concentration: 0.5 wt%). C) The insulating layer is fabricated using the polymer

resin (without added OS) to encapsulate the interconnect cables (height: 3 μm). D-F) Schematic illustrations for fabrication of biosensors: following construction of insulating electrode shank and base (height: 2 μm) from the polymer resin without added OS (A), D) enzyme-loaded sites are fabricated from OS composite resin containing glucose oxidase (GOx), E) construction of interconnect cables and contact pads using OS composite resin (without enzyme), F) fabrication of insulating layer. G-J) Optical micrograph representations of MPL-fabricated microstructures (scale bars: 50 μm). G) Representation of schematic (A), H) representation of schematic (D), I) representation of schematic (B) and (E), J) representation of schematic illustration (C) and (F). K-L) Pseudo-colored SEM micrographs of MPL-fabricated microelectrode at low and high magnifications, respectively (green represents polymer and red represents OS composite polymer). Scale bars in K and L are 100 μm and 50 μm, respectively.

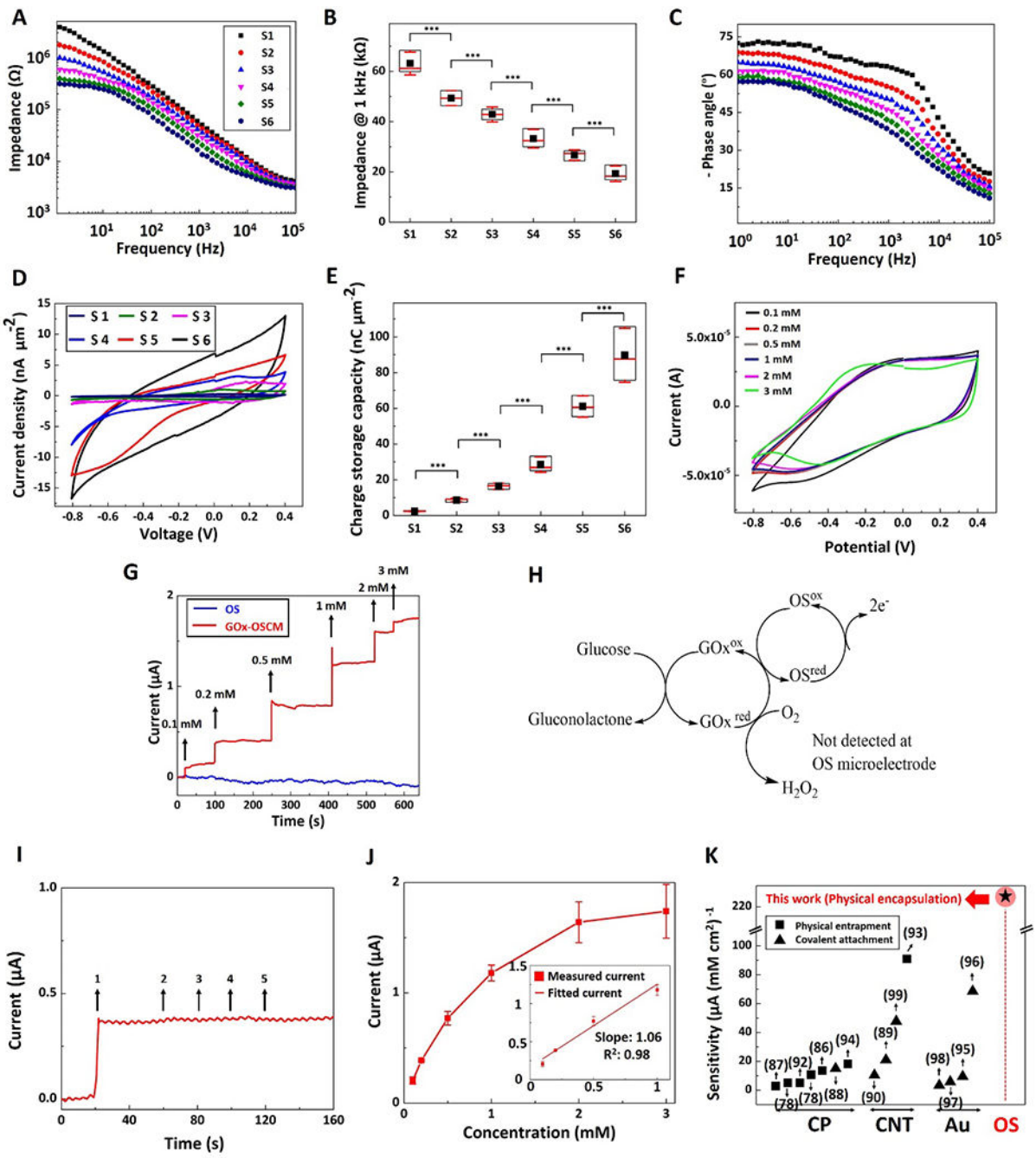


**Figure 6.**

Electrochemical characterization and glucose biosensing using MPL-fabricated composite microelectrode sites. A) Impedance magnitude over a frequency range of 1-$10^5$ Hz for electrode sites with diameters of: 1 µm (S1, black squares), 5 µm (S2, red circles), 10 µm (S3, blue up-sided triangles), 20 µm (S4, magenta down-sided triangles), 40 µm (S5, green diamond), and 80 µm (S6, dark blue hexagon). B) Impedance of microelectrode sites at 1 kHz. Data shown as mean ± SD, n=3, *** $p$<0.001 C) Phase angle of the impedance spectrum over the frequency range of 1-$10^5$ Hz. D) Cyclic voltammetry of microelectrode

sites, with potential swept from - 0.8 to 0.4 V and a scan rate of 0.1 V $s^{-1}$. E) Charge storage capacity of the microelectrode sites. Data shown as mean ± SD, n=3, *** $p$<0.001. F) Cyclic voltammetry of a microelectrode site in various glucose concentrations: 0.1 mM (black), 0.2 mM (red), 0.5 mM (grey), 1 mM (blue), 2 mM (magenta), and 3 mM (light green). G) Amperometric current response of OS (blue) and GOx-OSCM (red) composite microelectrodes to successive glucose addition at polarization potential of + 0.3 V vs. Ag/AgCl. H) Proposed detection mechanism of glucose using MPL fabricated GOx-OSCMs: electrons are transferred from glucose to the OS microelectrodes at + 0.3 V vs. Ag/AgCl. I) Amperometric current response of a GOx-OSCM composite microelectrode to addition of (1) glucose (0.2 mM), (2) acetaminophen (0.1 mM), (3) ibuprofen (0.1 mM), (4) ascorbic acid (0.1 mM), and (5) urea (0.1 mM), sequentially. J) The response curve (calibration curve) of the biosensor showed an operating range within 0.1-3 mM glucose concentration (dynamic range of current response 0-2 μA), with a sensitivity of 232.9 ± 22.5 μA $mM^{-1}$ $cm^{-2}$ between 0.1 and 1 mM as shown in figure inset. Data shown as mean ± SEM, n=4. K) Sensitivity of glucose biosensors (based on literature search) for different electroactive materials based on amperometric detection of glucose (CP: conducting polymers, CNT: carbon nanotubes, Au: gold, and OS: organic semiconductor). Black squares and black triangles demonstrate physical entrapment and covalent attachment, respectively. Star with red circle background represents the sensitivity of our novel sensor based on physical encapsulation of GOx in OS composite polymer). In (B) and (E), data are represented in box graphs where the black squares, red lines, and red whiskers demonstrate average, median, and standard deviation, respectively.